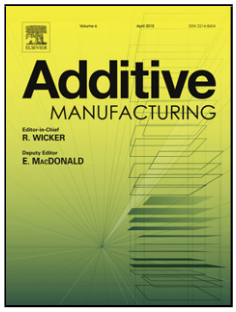


Title: Pilot Feedback Electronic Imaging at Elevated Temperatures and its Potential for In-Process Electron Beam Melting Monitoring

Authors: Hay Wong, Derek Neary, Eric Jones, Peter Fox, Chris Sutcliffe

PII: S2214-8604(18)30857-1
DOI: https://doi.org/10.1016/j.addma.2019.02.022
Reference: ADDMA 654

To appear in:

Received date: 22 October 2018
Revised date: 15 February 2019
Accepted date: 26 February 2019

Please cite this article as: Wong H, Neary D, Jones E, Fox P, Sutcliffe C, Pilot Feedback Electronic Imaging at Elevated Temperatures and its Potential for In-Process Electron Beam Melting Monitoring, *Additive Manufacturing* (2019), https://doi.org/10.1016/j.addma.2019.02.022

# Pilot Feedback Electronic Imaging at Elevated Temperatures and its Potential for In-Process Electron Beam Melting Monitoring

**Authors: Hay Wong[a], Derek Neary[a], Eric Jones[b], Peter Fox[a], Chris Sutcliffe[a]**

**[a]School of Engineering, University of Liverpool, The Quadrangle, Brownlow Hill, United Kingdom L69 3GH**

**[b]Jones Consultancy, Ardlahan, Kildimo, Co. Limerick, Ireland**

**Corresponding author's email: Hay Wong – hay.wong@liv.ac.uk**

## Abstract

Electron Beam Melting (EBM) is an increasingly used Additive Manufacturing (AM) technique employed by many industrial sectors, including the medical device and aerospace industries. The application of this technology is, however, challenged by the lack of process monitoring and control system that underpins process repeatability and part quality reproducibility. An electronic imaging system prototype has been developed to serve as an EBM monitoring equipment, the capabilities of which have been verified at room temperature and at 320+10°C. Nevertheless, in order to fully assess the applicability of this technique, electronic imaging needs to be conducted at a range of elevated temperatures to fully understand the influence of temperature on electronic image quality. Building on top of the previous electronic imaging trials at room temperature, this paper disseminates the essential step changes to allow high temperature electronic imaging: (1) modification of a signal amplifier to deal with high electron beam current during electron beam heating, and (2) design of an open-source electron beam heating algorithm to maximise flexibility for user-defined heating strategy. In this paper, electronic imaging pilot trials at elevated temperatures, ranging from room temperature to $650°C$, were carried out. Image quality measure Q of the digital electron images was evaluated, and the influence of temperature was investigated. In this study, raw electronic images generated at higher temperatures had greater Q values, i.e. better global image quality. It has been demonstrated that, for temperatures between$30°C - 650°C$, the influence of temperature on electronic image quality was not adversely affecting the visual clarity of image features. It is thus envisaged that the prototype has a potential to contribute to in-process EBM monitoring, and this paper has served as a

crucial precursor to the ultimate goal of carrying out electronic imaging under real EBM building condition.

**Keywords: Additive Manufacturing; Electron Beam Melting; In-Process Monitoring; Quality Control; Electronic Imaging**

## 1. Introduction

Electron Beam Melting (EBM) is an Additive Manufacturing (AM) technique that makes use of an accelerated electron beam to melt metallic powder on a layer-by-layer basis, forming components based on the geometries of the imported three dimensional Computer Aided Design (CAD) models [1]. The ability of the EBM process to form components from metallic powder arises from electron interactions with metallic materials. When an electron beam is accelerated by an anode, focused onto a powder bed by an electromagnetic focusing coil and subsequently deflected to specific locations by an electromagnetic deflection coil, the electrons penetrate the powder particles, whereupon they slow down and convert their kinetic energy into thermal energy. If the energy input is sufficient, the temperature of the powder particles rises above their melting point and solid-to-liquid phase transformation is initiated. When the beam is raster-scanned across the preheated powder bed in a tightly controlled, predefined pattern, melt tracks are solidified to form fully dense cross sections of the desired components. This process is repeated with the additional requirement that the underlying solid is also partially re-melted to ensure adequate bonding between the underlying and newly formed layers ensuring that full density is achieved.

It is thought that the technique shows great promise in the manufacture of orthopaedic implants and aerospace components. In an evaluation study on powder-based EBM technology, it was concluded that the EBM process would have the flexibility to enable the manufacture of a wide range of complex and difficult-to-fabricate aerospace and biomedical components [2]. The increased design freedom of the EBM process enables the economic manufacture of porous bone ingrowth surfaces for orthopaedic implants [3] whilst

the reduced thermal residual stress and the high-vacuum process environment is beneficial for the production of aircraft components [4]. Nevertheless, both of these industries are highly regulated and their standard manufacturing processes are well established [5, 6]. It is thought that despite the perceived benefits of the EBM process, the transition from the current standard manufacturing techniques to a layered manufacturing approach would not be possible unless a rigorous EBM process monitoring and validation system was available for real-time control [7].

Academic research communities have built different monitoring systems to assess the quality of the EBM process. These systems make use of infrared (IR) (wavelength between $700nm$ and $1mm$), visible light (wavelength between $400nm$ and $700nm$), and feedback electrons, i.e. Secondary Electrons (SE) and Backscattered Electrons (BSE) as feedback monitoring signals. Table 1 summarises the monitoring systems developed.

**Table 1** Monitoring systems developed for the EBM process

| Process Attribute Monitored | Monitoring Method | Process Artefacts | Sensor | Reference |
|---|---|---|---|---|
| Processing area surface temperature | Thermal imaging | IR | Microbolometer | [8 – 11] |
| Melt pool geometry | Thermal / optical imaging | IR / visible light | Microbolometer / CMOS sensor | [12 –14] |
| Processing area topography | Thermal imaging / electronic imaging | IR / electrons | Microbolometer / electrically conductive surface | [15 - 22] |

Monitoring attempts were made on the Arcam S12 EBM machines by Raplee et al with a FLIR 7600 mid-wave IR camera [8], Cordero et al with a multi-wave pyrometer [9],

and Price et al with a LumaSense MCS640 near-IR camera [12]. In addition, Arcam A2 machines were used by Cordero et al, Rodriguez et al and Mireles et al with FLIR SC645 IR cameras [9, 10, 16], Scharowsky et al with a Photron Fastcam SA3 visible light camera [14], and Schwerdtfeger et al with a FLIR A320 IR camera [18]. Moreover, an Arcam A1 EBM machine was interfaced with an in-house developed digital electronic imaging system prototype by Wong et al [21, 22], and a NASA EBF3 machine was interfaced with a Prosilica GC1380H near-IR camera by Zalameda et al [11].

When compared to thermal and optical imaging, it has been shown that electronic imaging has the potential to offer superior flexibility on image Field of View (FOV) and image magnification [21]. Although the electronic image quality has been verified at room temperature and 320+10°C [22], the image quality is still yet to be evaluated at a full range of elevated temperatures (room to in-process EBM monitoring temperature) to understand the influence of temperature on feedback electron generation and the potentially on thermal noise [23]. The applicability of electronic imaging in EBM monitoring cannot be fully explored without extending the investigation into the influence of temperature on electronic image quality.

In order to reduce the complexity of carrying out multi-layer electronic imaging under real EBM condition, it is proposed that intermediate trials should be conducted beforehand as a precursor: single-layer electronic imaging at a range of temperatures increasing in value towards the actual in-process monitoring temperature of a chosen demonstration material. Ti-6Al-4V alloy was selected to be the demonstration material for this study due to its popularity in the field of AM, aerospace and medical industries [24, 25].

## 2. Materials and Methods

### *2.1 Analysis of Imaging at Eleveted Temperatures and Prototype Modification*

A bespoke digital electronic imaging system prototype was interfaced with an Arcam A1 EBM machine (GE Additive, USA), hereafter referred to as the EBM machine, to carry out imaging trials at elevated temperatures, as depicted in Figs. 1(a) and (b). The prototype consisted of an electron sensor (modified Arcam heat-shield frame and plates), a data logger (Arduino DUE microcontroller break-out board), signal amplifier and image generation software and was designed to generate digital electronic images from the Secondary

Electrons (SE) and Backscattered Electrons (BSE), originating from the interactions between the machine's primary electron beam and the processing area [22].

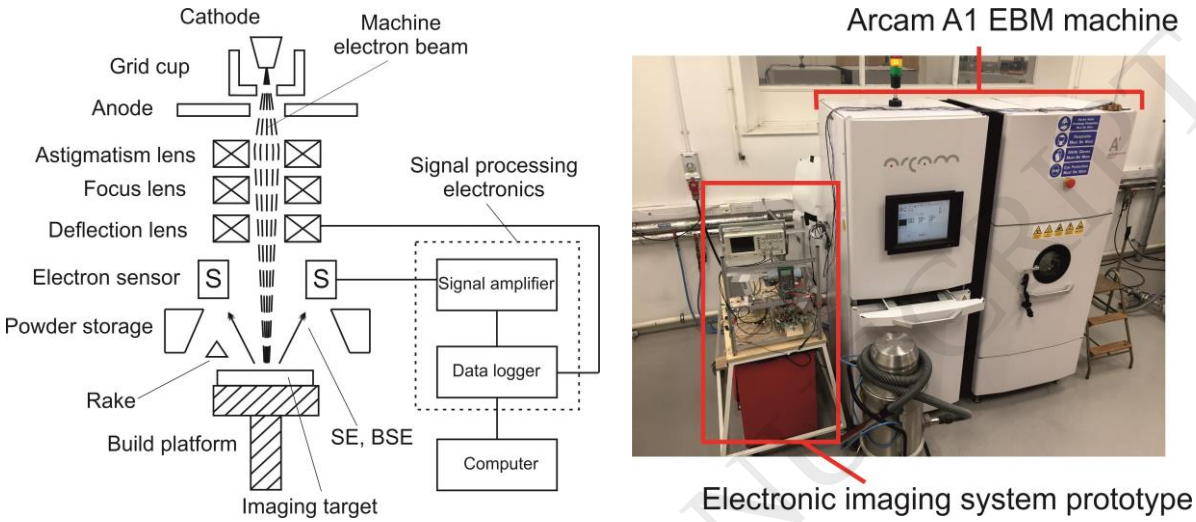


(a) Adapted schematic [21] (b) Laboratory installation

**Fig. 1** Electronic imaging system prototype interfaced with an EBM machine

Carrying out image generation at higher temperature is thought to introduce at least four poential challenges: (1) the yield of SE and BSE might vary with temperature; (2) undesired thermionic electrons from the imaging target might lower the Signal-to-Noise Ratio (SNR) of the feedback electron signal for imaging; (3) the signal amplifier (illustrated in Fig, 1(a)) would be required to suppress the SE and BSE signals during the electron beam heating stage, and (4) the effect of temperature on the feedback electron sensor. In EBM, different metals are processed using different process parameters. In this study, Ti-6Al-4V alloy was chosen as the demonstration material, and throughout the course of experimentation, the powder bed on the processing area was maintained at approximately $700°C$ achieved by electron beam heating [26].

With regard to the first challenge, the key factor is to determine the influence of temperature on SE and BSE yields. Literature shows that temperature has little to no effect on the yield of SE due to the scale factor of the kinetic energy of an atom, $kT$ (where $k$ is the Boltzmann's constant), which is small when comapred to the average SE or BSE energy [27].

In general, the average energy of a SE is $2-5eV$. By convention, the minimum energy of a BSE is $50eV$ [28] and the primary electron in an EBM machine has an energy of $60keV$ [29]. At $700°C$, $kT$ has a value of approximately $0.084\ eV$, only 5% of the least energetic SE. As SE and BSE are generated from interactions between a primary electron beam and its target atoms [30], at $700°C$, thermal vibration (proportional to the kinetic energy, $kT$) of atoms in the target was not expected to affect the combined yield of both SE and BSE, as defined in Eq. 1. This challenge regarding SE and BSE yield at elevated temperatures is thought to be insignificant to this study.

$$\gamma_{SE,BSE} = \frac{I_{SE} + I_{BSE}}{I_{PE}}$$

$$\gamma_{SE,BSE} = \frac{I_T}{I_{PE}} \quad (1)$$

Where

$\gamma_{SE,BSE}$ is the combined SE and BSE yield, $I_{SE}$ (A) and $I_{BSE}$ (A) are the SE and BSE generated from interactions between a primary beam and the imaging target, $I_T$ (A) is the total raw SE and BSE current signal – the feedback signal, and $I_{PE}$ (A) is the primary beam current firing at the imaging target.

Regarding the second challenge, the issue with noise during electronic imaging at high temperature has been observed and disseminated by Nakamura et al [31] and Gregori et al [32]. Nakamura et al reported that a heating stage (tungsten wires as heating element) emitted themionic electrons, i.e. image noise, during electronic imaging at around 900 °C. Gregori et al faced similar challenges and reported that, even when their tantalum heating wires were encapsulated by metallic cylinders, thermioinc electron noise from the imaging sample and the metallic cylinders were still recorded. These thermioinc electron emissions can be described by the Richardson Law [32], which is given in Eq. 2.

$$J_C = AT^2 \exp(-E_W/kT) \quad (2)$$

Where

$J_C$ ($Amm^{-2}$) is the current density of the emitted thermionic electrons, A ($Amm^{-2}K^{-2}$) is a material-dependent constant, T (K) is temperature, $E_W$ (eV) is the material work function, and k ($eVK^{-1}$) is the Boltzmann constant.

At high temperatures, significant reduction in the electronic imaging signal SNR was observed. This led Nakamura et al and Gregori et al to develop their own thermionic electron filters. The working principle of their filters is to suppress/ repel the undesired low energy thermionic electrons by a biased grid electrode [31, 32]. As tungsten/ tantalum and the common elements in typical metal AM alloys, i.e. Co, Cr, Fe, Mo, Ni, Ti and V, all have similar work functions in the range of 4.09 to 4.84eV [33], it is believed that the issue with thermionic electron noise might occur during in-process EBM monitoring with electronic imaging, when the imaging target (this study)/ powder bed (in real build) are brought to high temperatures.

Regarding the third challenge, the key factor is to suppress input signals to the prototype data logger. The input signal needs to be less than $3V$ due to the choice of data logger in this experiment, and the signal level should be suppressed when imaging is not taking place. The signal amplifier in the system protoype processes the SE, BSE and noise signals, in the form of electric current, before feeding it into the data logger, as depicted in Fig. 1(a). Eq. 3 defines how the noise is filtered out from the feedback electron signal, and how signal amplification is determined by the amplfier gain and electrical resistance involved.

$$V_{amp} = G \times R \times (I_{Signal+N} - I_N)$$

$$V_{amp} = G \times R \times I_T \quad (3)$$

Where

$V_{amp}$ (V) is the differentially amplified voltage signal fed into the data logger, G is the gain of the signal amplifier, R (Ω) is the resistance used to convert the electrical current to a voltage in the differential signal amplifier, $I_{Signal+N}$ (A) is the total raw feedback electron signal with noise – sampled by the signal-capturing heat-shield plates on the electron sensor, and $I_N$ (A) is the noise – sampled by the noise-capturing heat-shield plates on the electron sensor.

The need for signal suppression arises from the passive nature of the electron sensor. The sensor captures and send signals to the data logger at all times, during both the heating and imaging stages. The primary beam current, $I_{PE,}$ value assigned for the two stages were different and thus it is expected that the total feedback signal, $I_T$, would be different, even with a constant combined feedback electron yield $\gamma_{SE,BSE}$. The feedback signal should be suppressed during heating and amplified during imaging. In order to handle the feedback signal correctly, modification to the signal amplifier was carried out by introducing two indepentent gain options for the two stages respectively. Table 2 summarises the modified amplifier settings for the two stages and Fig. 2 is a block diagram illustrating the modified signal amplifier.

**Table 2** Electronic imaging system prototype signal amplifier settings during heating and imaging. Values rounded to 2 s.f.

| Signal Amplifier Parameter | Value (Heating) | Value (Imaging) |
|---|---|---|
| Primary electron beam current $I_{PE}$ (mA) | 48 | 1.0 |
| Estimated feedback electron yield $\gamma_{SE,BSE}$ | 0.3 | 0.3 |
| Estimated raw feedback signal $I_T$ (mA) | 14 | 0.3 |
| Electrical resistance R (Ω) | 9.9 | 1000 |
| Signal amplifier gain G | 1.1 | 10 |
| Estimated amplifier output $V_{amp}$ (V) | 0.16 | 3.0 |

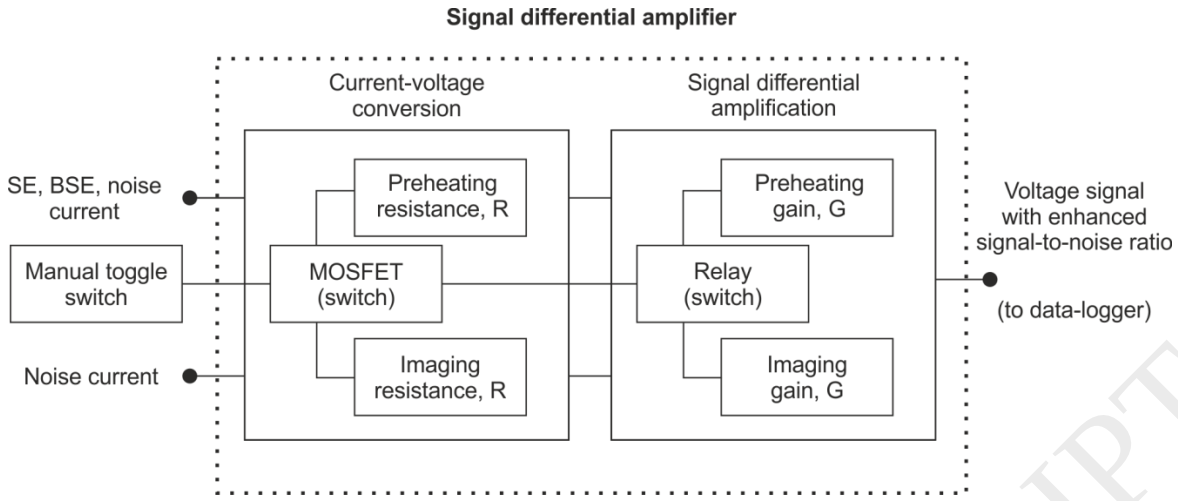


**Fig. 2** Modified signal differential amplifier

With regard to the forth challenge, the key factor is to estimate the increase in the electron sensor electrical resistance due to temperature by applying Eq. 4 [34].

$$R_1 = R_0[1 + \alpha_{Fe}(T_1 - T_0)] \quad (4)$$

Where

$R_i$ (Ω) is the resistance at Ti, and $\alpha_{Fe}$ ($°C^{-1}$) is the temperature coefficient of resistance for iron, $\alpha_{Fe}$= 0.0065 $°C^{-1}$.

The elecrron sensor in the electronic imaging system protoype was a modified Arcam stainless steel heat-shield frame and two sets of stainless steel plates (one for capturing feedback electrons, the other for capturing noise). The sensor resistance at room temperature was measured to be 0.6 Ω. If assuming in the worst-case scenario, the sensor is at the same temperaure as the processing area, which is 700 °C, and using the temperature coefficient of resistance for iron to represent stainless steel, then the resistance of the sensor at 700 °C is estimated to be 3.21 Ω. Referring to the parameters given in Table 2, the updated amplifier electrical resistances are 13.11 Ω (Heating) and 1003.21 Ω (Imaging), and the updated estimated amplifier outputs are 0.2 V (Heating) and 3V (Imaging). As a result, the increase in sensor electrical resistance due to temperature is expected to have insignificant effect on the amplfier output voltage in this pilot study, in which only single-layer electronic imaging was carried out at elevated temperatures for a duration of less than 2 hours. Nevertheless, testing

of the sensor under high temperature for long hours, i.e. 100+ hours, should be conducted in future studies under real EBM building condition to further verify the effect of temperature on the sensor.

*2.2 Controlled Heating Software Development and Verification Trial*

A piece of custom heating software was developed in the open-source Python programming language to achieve controlled heating with the use of the EBM machine electron beam. The software outputs a cutter location file (.clf file). The .clf heating file can be imported to the Arcam Build Assembler ® software to generate an Arcam build file (.abf file). This .abf heating file can then be imported to and read by the Arcam EBM Control ® software, alongside other typical Arcam design build files. User-defined electron beam theme can be assigned to the custrom heating file, just as the typical wafer/ melt themes are appled to the build support/ build design models. When the heating algorithm is in use, the beam would be directed to raster scan a heating target to increase the temperature uniformly from room temperature to 700°C, for a typical Ti-6Al-4V build. Fig. 3(a) describes the working principle of the heating software whilst Fig. 3(b) depicts typical sets of scan lines generated. Although the scan line pattern shown in Fig. 3(b) is similar to that used by the EBM machine manufacturer, Arcam AB, the true value of this custom software lies in the flexibility available for research and development purposes. The distinct benefits of the current version of software include: (1) there is no downtime assigned for heat-shield out-gassing. If the Arcam's "start-plate heating" algorithm is used instead, there is no way for the user to turn-off this waiting time (15-20 minutes). In this pilot heating trial, no real components were built, there was no need to wait for the heat-shield to complete out-gassing to stabilise the chamber pressure level, (2) the user can freely define the scan line spacing and the number of scan line sets. This enables the user to investigate into the best heating strategy to maximise heating efficiency, rather than being constrained by what is provided by the machine manufacturer, and (3) the user has full control to define different heating areas across the processing area, thus the software provides flexibility for local heating across the processing area, opening opportunities to look into the effect of different heating strategies on mechanical properties of components in a single EBM build.

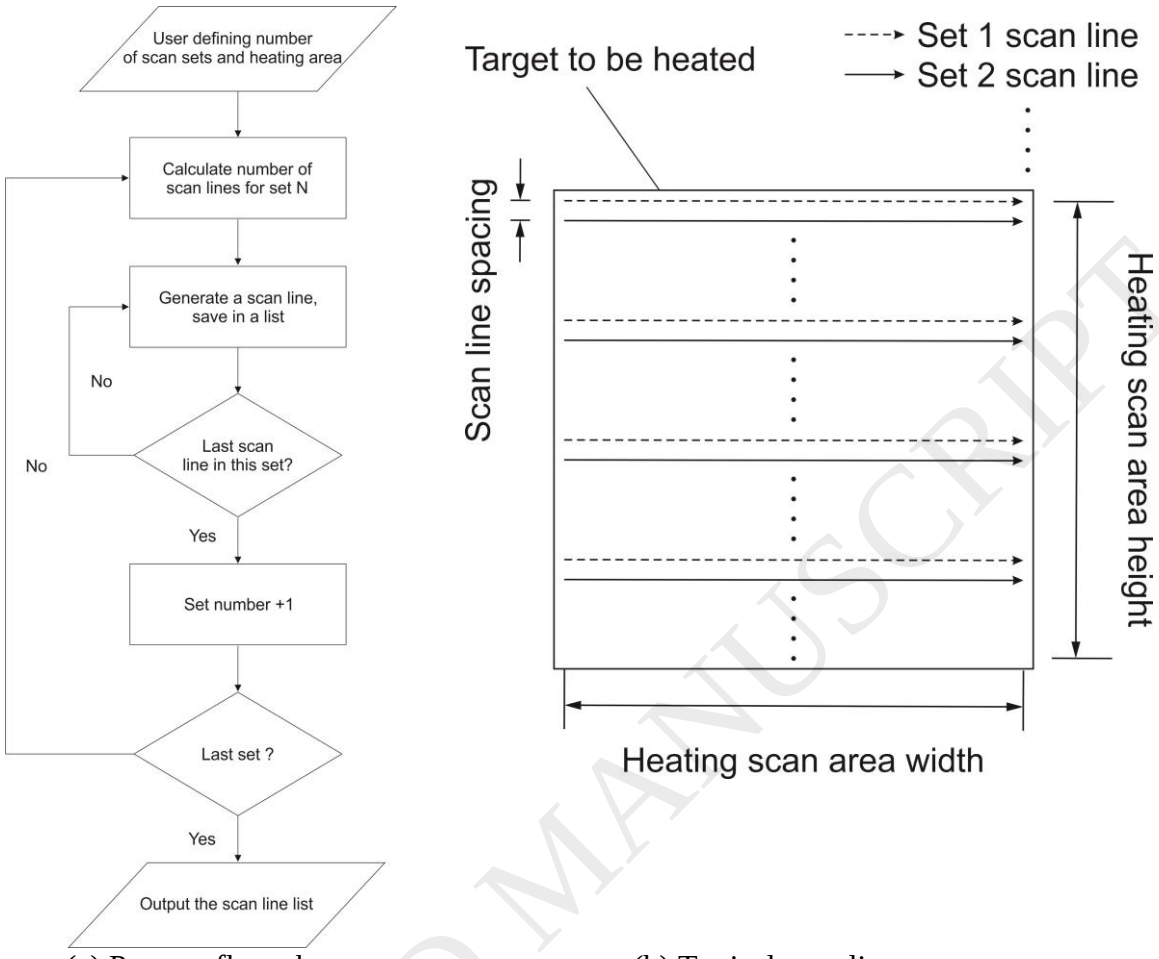


(a) Process flow chat (b) Typical scan line output

**Fig. 3** Controlled heating software

A verification trial was conducted upon completion of the heating software development. The software was applied to the EBM machine and the machine electron beam was used to heat up a stainless steel plate, i.e. heating target, by raster scanning across it in a pattern defined by the software. Temperature data of the heating target was measured, processed and recorded by a thermocouple (TC), TC amplifier and a microcontroller respectively. Fig. 4(a) and (b) show the verification setup. Fig. 4(a) shows how the heating target, TC and microcontroller are connected to each other. Fig. 4(b) shows the design of the stainless steel plate, used as both a heating target in the verification trial and an imaging target in the imaging trials at a later stage. This plate, hereafter referred to as target plate, was made of one single material to avoid non-uniform deformation due to differences in thermal expansion coefficient during heating. Nine location markers and 27 pockets were machined

across the plate. These features were used to develop image contrast during electronic imaging, allowing image quality to be evaluated. Prior to the verification trial, the target plate was processed as part of the development of the heating software. Multiple pilot heating scans with various electron beam parameters were carried out across the middle of the plate. These developmental activities led to surface damage. During pilot electron beam heating, the beam traced out the target plate, leaving horizontal markings behind. In an attempt to undo the damage, the target plate was bead blasted manually with the Guyson Formula 1200 blast system (Guyson, UK), with 60-80 grit aluminium oxide abrasive, to smooth out its surface texture.

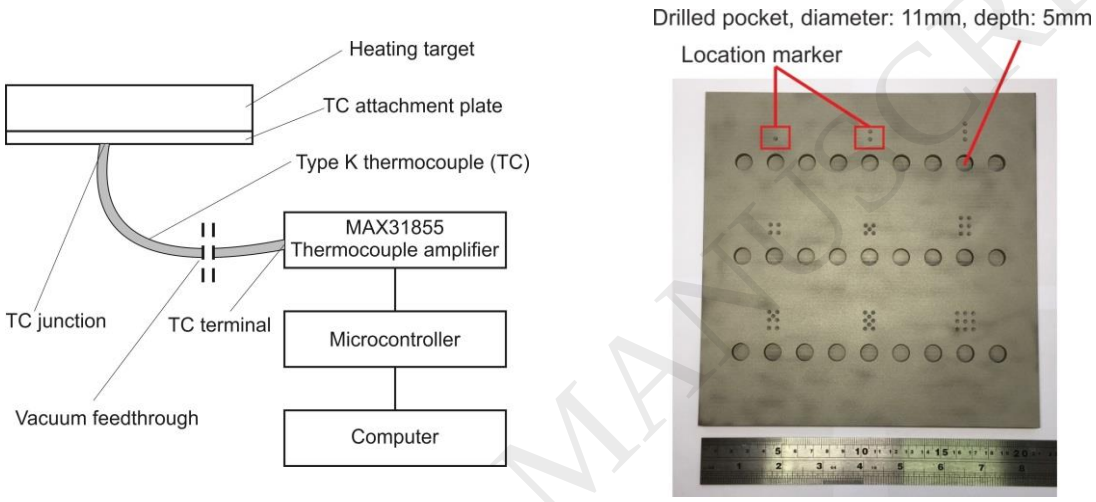


(a) Schematic of the setup (b) The heating target plate

**Fig. 4** Heating software verification setup

Table 3 details the controlled heating verification trial configuration. The electron beam speed, current and focus offset were chosen based on the beam parameters from the EBM machine standard pre-heating theme. $700°C$ was chosen to be the temperature goal. Figs. 5(a) and (b) show the heating sequence generated by the controlled heating software for its verification.

**Table 3** Controlled heating verification trial configuration

| Controlled Heating Verification Trial Parameters | Value |
|---|---|
| Heating target dimension ($mm^3$) | $210 \times 210 \times 10$ |

| | |
|---|---|
| Heating target material | Stainless steel |
| TC attachment plate dimension ($mm^3$) | $200 \times 200 \times 2$ |
| TC attachment plate material | Stainless steel |
| Heating area ($mm^2$) | $200 \times 200$ |
| Scan line spacing (mm) | 2.5 |
| Number of scan lines per heating sequence | 1760 |
| Duration of each heating sequence (s) | 10 |
| Electron beam heating current (mA) | 48 |
| Electron beam heating focus offset (mA) | 80 |
| Electron beam heating scan speed ($mms^{-1}$) | 35000 |
| Goal maximum temperature (°C) | 700 |

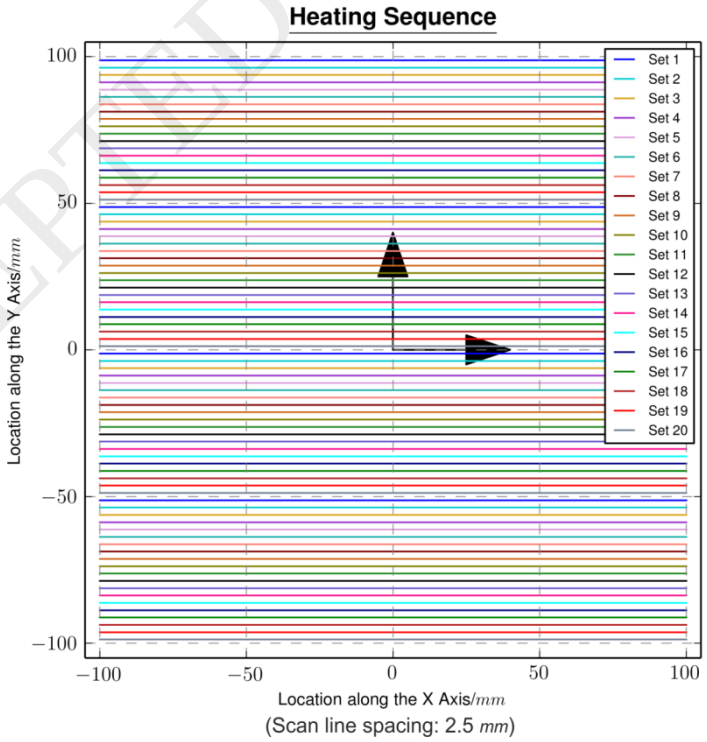

(a) Controlled heating software output schematic

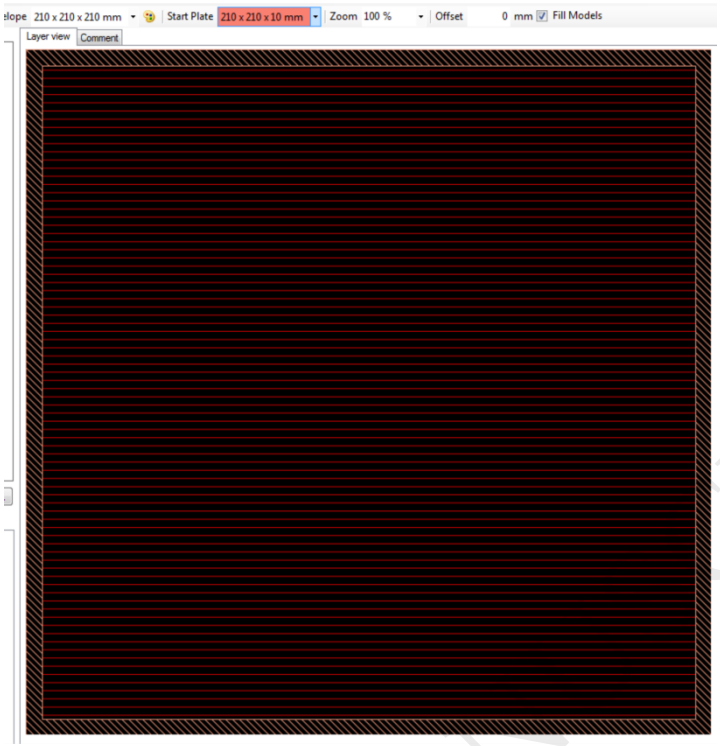


(b) Software output imported to the Arcam Build Assembler ® software

**Fig. 5** Heating sequence software verification

In the verification trial, the target plate was successfully heated from room temperature to $700°C$ as shown in Fig. 6. The trial result demonstrates that the controlled heating software is capable of bringing the target plate temperature up to the in-process EBM monitoring temperature for Ti-6Al-4V.

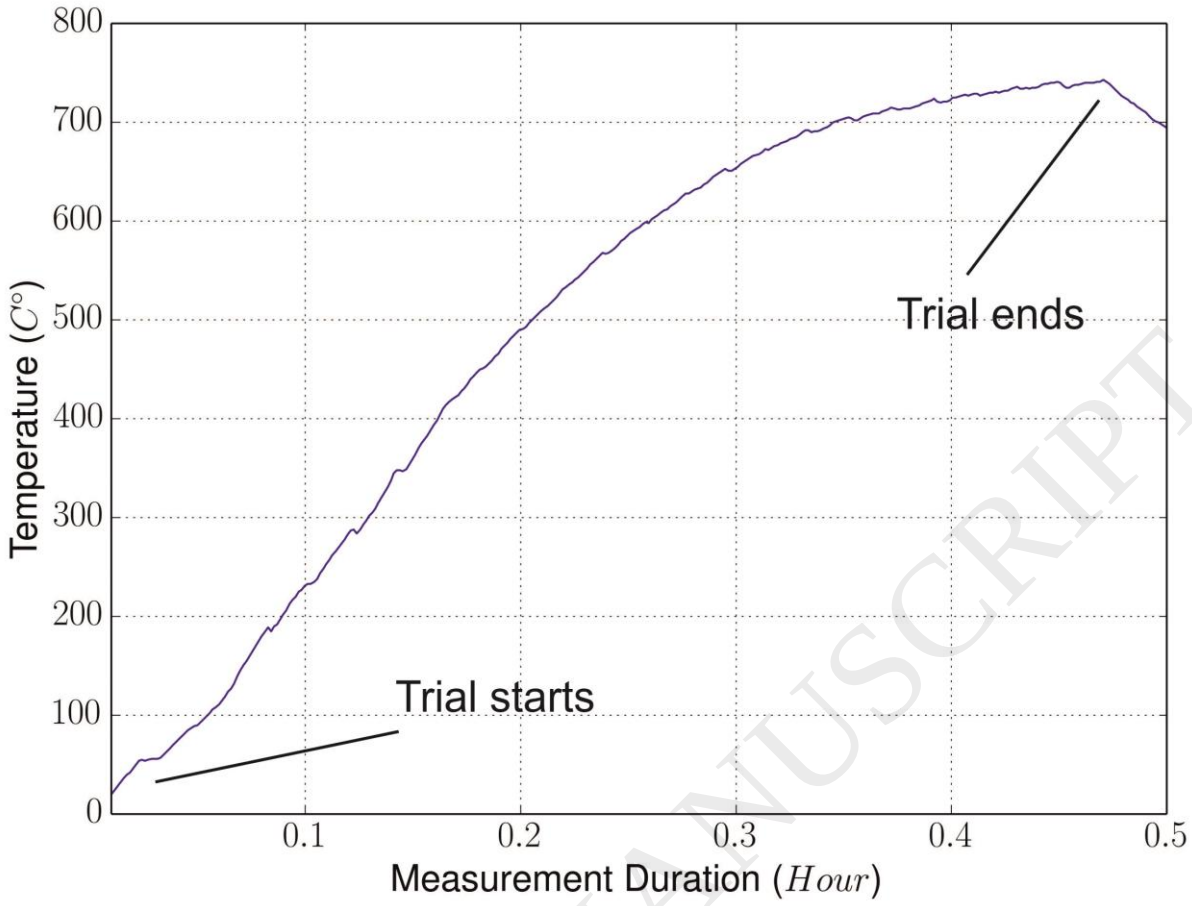


**Fig. 6** Target plate temperature profile during controlled heating sequence verification

*2.3 Electronic Image at Elevated Temperatures Experimental Setup*

Upon successful verification of the controlled heating software, electronic imaging was carried out at elevated temperatures with the electronic imaging system prototype and the EBM machine shown in Figs. 1(a) and (b). The target plate shown in Fig. 4(b) was used as an imaging target. The verification temperature measurement setup (Figs. 4(a) and (b)) and controlled heating configuration (Table 3) were used to bring up the imaging target temperature during the experiment. Table 4 gives the experimental configuration of the prototype and the EBM machine. The list below gives an overview of the experimental steps carried out:

1. Heat up target plate to a selected, intermediate temperature
2. Screenshots of the EBM machine computer taken, with chamber light switched on/off (images captured by the EBM machine KPC-S500B optical camera (KT&C, USA))

3. 5 x electronic imaging conducted with machine chamber light switched off, and data handling (saving time-series feedback electronic signal from oscilloscope, changing image file name, allocate to specific folder)
4. Reset EBM machine to carry out electron beam heating



**Table 4** Prototype and EBM machine configurations for imaging at elevated temperatures

| Imaging Experiment Parameters | Value |
|---|---|

| | |
|---|---|
| Machine chamber vacuum level (mbar) | $10^{-3}$ |
| Electron beam imaging current (mA) | 1 |
| Electron beam imaging scan speed ($mms^{-1}$) | 11880 |
| Electron beam imaging focus offset (mA) | 0 |
| Signal amplifier gain | 10 |
| Data logger input / output range (V) | $0\ to + 3.3$ |
| Data logger sampling frequency (Hz) | $118.8k$ |
| Sample resolution (bit) | 8 |
| Data logger sampling bit rate (bps) | $950.4k$ |
| Imaging area ($mm^2$) | $180 \times 180$ |
| Imaging scan spacing (mm) | 0.1 |
| Scan lines in 1 image frame | 1800 |
| Image frame time (s) | 27 |
| Image size (pixel) | $1800 \times 1800$ |
| Image bit depth | 256 |
| Imaging temperatures (+10°C) | $30/200/350/450/700$ |

## 3. Results

*3.1 Imaging Target Temperature Profile during Experiment*

The target plate temperature was monitored by a TC and its peripheral electronics during the experiment. Fig. 7 depicts the target plate temperature profile. It shows that the target plate temperature ramps up from room temperature to up until $700°C$. The figure illustrates that electronic images are generated at five different temperatures throughout the experiment. The figure also shows that the target plate temperature drops during imaging. Moreover, the rate of temperature drop increases as temperature rises. In addition, Fig. 7 shows that, at each temperature step, it took 9 to 15 minutes to generate five electronic images, handle data, and reset the EBM machine for heating.

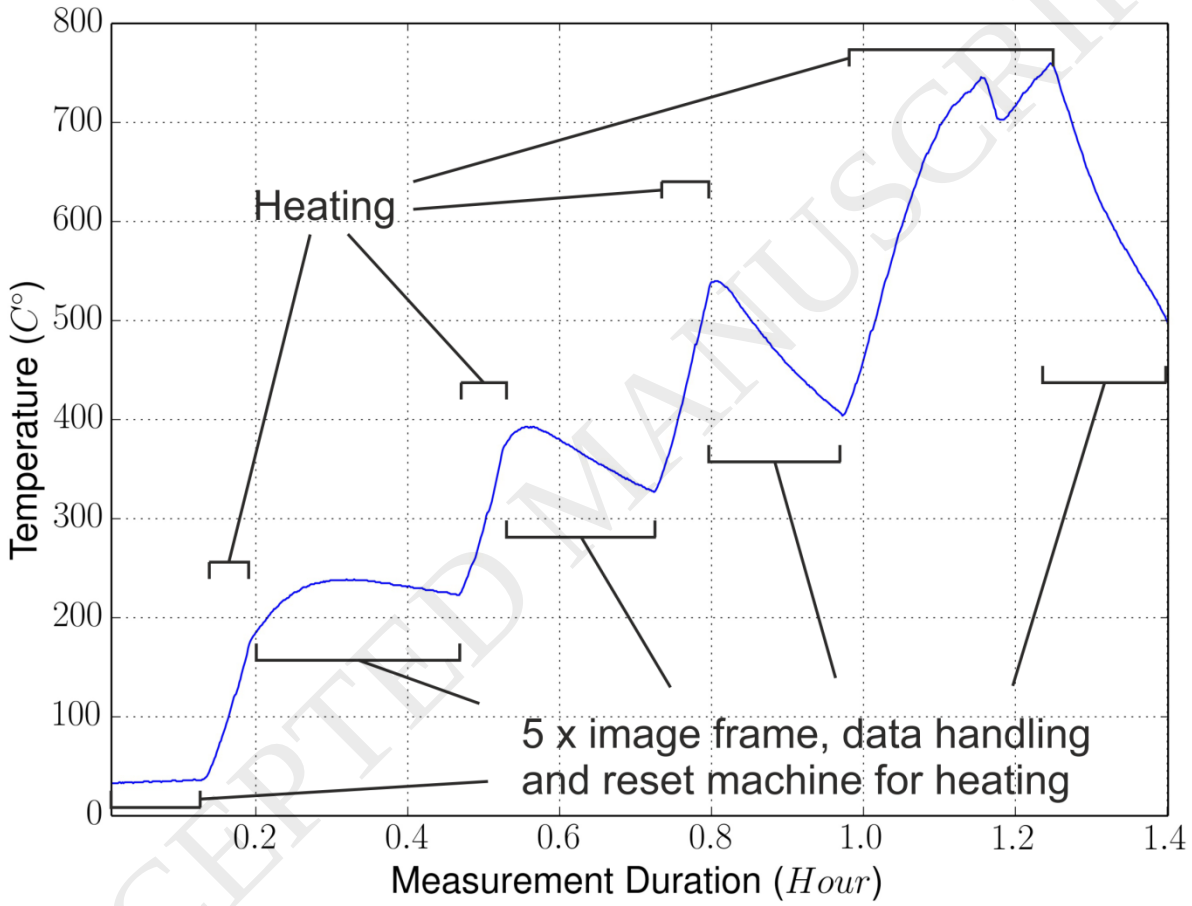


**Fig. 7** Target plate temperature profile during experiment

*3.2 Optical Images from the Arcam A1 EBM Machine Camera*

During experiments, screenshots of the EBM machine computer were captured at various elevated temperatures to demonstrate the quality of typical thermal/optical images. Figs. 8(a)-(d) are the typical screenshots captured. Figs. 8(a) and (b) were captured at 30+10°C with the chamber light switched off and on; Figs. 8(c) and (d) were captured at 650+10°C with the chamber light switched off and on. A bright circular spot in the centre of the target plate can be observed in Figs. 8(a) and (c), when the chamber light was switched off. The bright spot is no longer visible when the chamber light is on, as demonstrated by Figs. 8(b) and (d). Reader should note that the machine camera was not directly situated above the processing area, the optical images thus suffer from keystone distortion. The image scale bar should only be used as a rough guide to dimension, whilst true dimension of the target plate is given in Fig. 4(b).

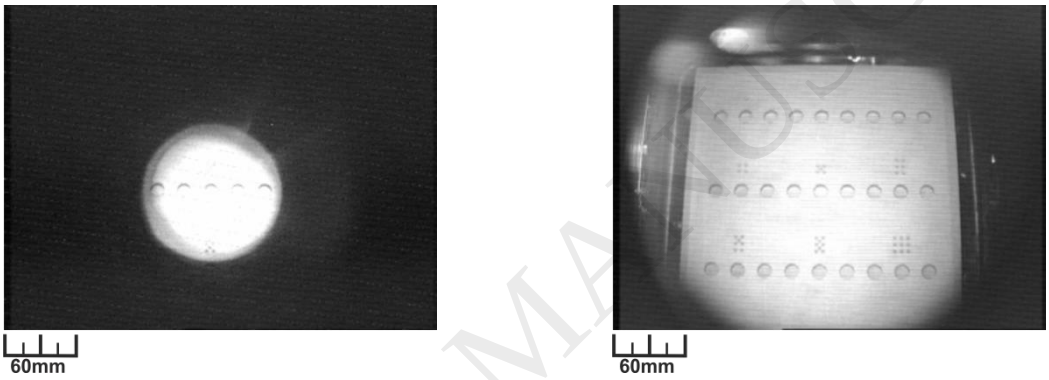


(a) 30+10°C, light off (b) 30+10°C, light on

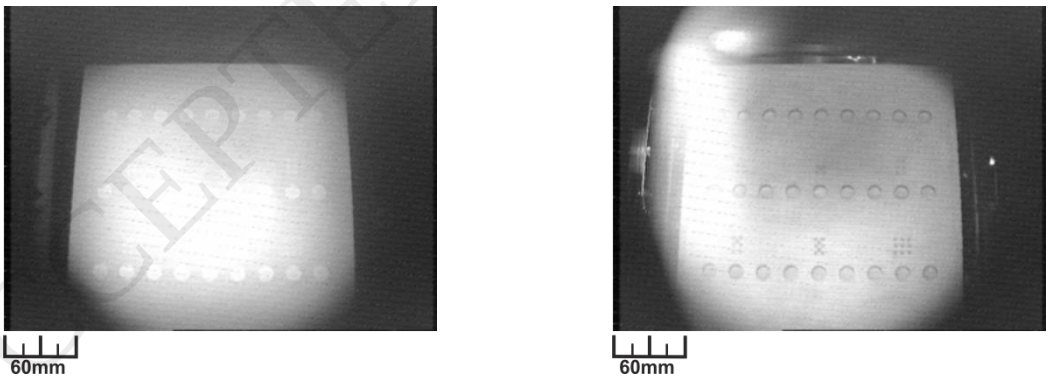


(c) 650+10°C, light off (d) 650+10°C, light on

**Fig. 8** Computer screenshots of the target plate taken from the machine camera

*3.3 Digital Image Processing*

Raw digital electronic images were generated from the electronic imaging experiment. In order to generate processed electronic images, noise was removed by applying a median filter, and image contrast was enhanced by carrying out histogram equalisation. Eq. 5 [35] and Eq. 6 [35] define the median filter and histogram equalisation functions used respectively. The median filter applied had a user-defined neighbourhood area of a circle with radius of two pixels. The histogram equalisation was carried out with a user-defined saturated pixel value of 0.3%, allowing 0.3% of the total pixels to become saturated.

$$\hat{f}(x,y) = \underset{(s,t)\in S_{xy}}{median}\{g(s,t)\} \tag{5}$$

Where

$\hat{f}$ (x,y) is the pixel-value of the filtered image at (x,y), g(s,t) is the pixel-value of the raw image at (s,t), and $S_{xy}$ represents the set of coordinates within a user-defined area of an image

$$y_k \triangleq \left\lfloor \left[ (L-1)\sum_{i=0}^{k} h(i) \right] + 0.5 \right\rfloor \qquad k = 0, 1, 2, \ldots\ldots, L-1 \tag{6}$$

Where

L is the bit-depth in an image, k is the pixel-value within the bit-depth, L, h(i) is the normalised histogram which gives the probability of occurrence of pixel-value, I, $\sum_{i=0}^{k} h(i)$ is the cumulative probability distribution of the normalised histogram, and $y_k$ is an integer, the equalised number of pixel with a pixel-value of k

*3.4 Electronic Images from the Prototype*

Electronic imaging was conducted at five elevated temperatures, covering a range of $30°C$ to $650°C$. Five electronic images were generated at each temperature step. Figs. 9(a)-(e) present the typical raw electronic images generated. Figs. 10(a)-(e) on the other hand, present the typical processed electronic images with noise removed and contrast enhanced. The two processed electronic images generated at 30+10°C (Fig. 10(a)) and 200+10°C (Fig. 10(b)) show a darker area across the middle of the target plate.

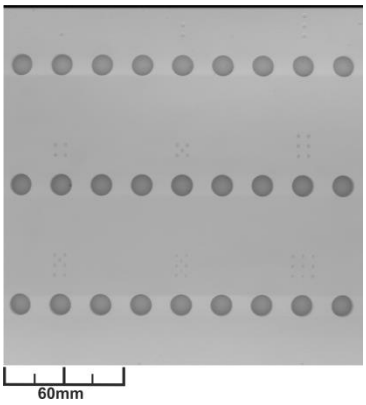


(a) 30+10°C

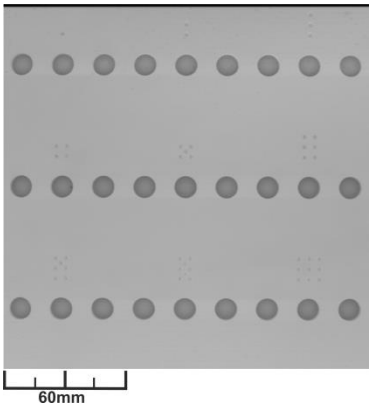


(b) 200+10°C

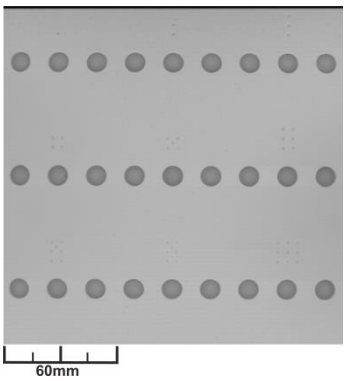


(c) 350+10°C

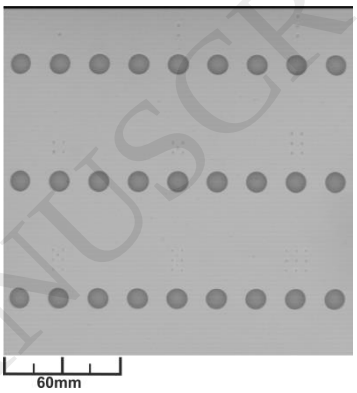


(d) 450+10°C

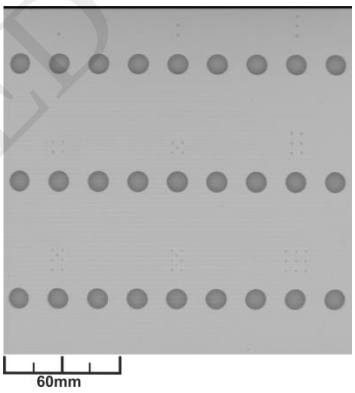


(e) 650+10°C

**Fig. 9** 8-bit, 1800 $pixel$ × 1800 $pixel$ ($row$ × $column$) digital electronic images (raw) covering an imaging area of 180$mm$ × 180$mm$ ($W$ × $D$) in the EBM machine processing area, generated at various temperatures with chamber light off

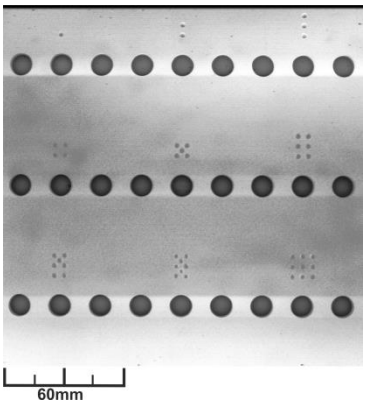


(a) 30+10°C

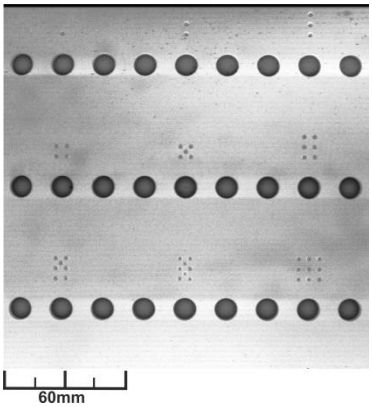


(b) 200+10°C

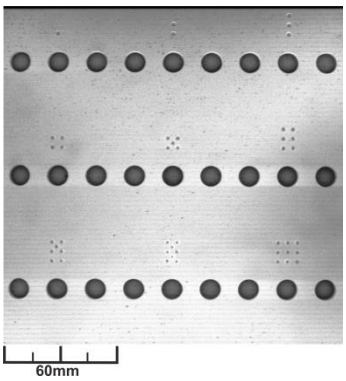


(c) 350+10°C

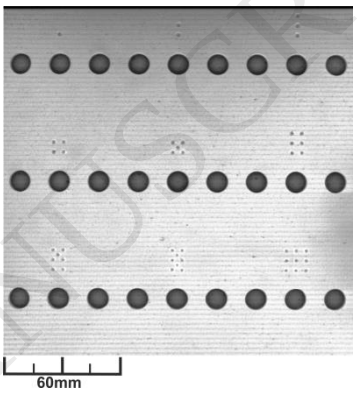


(d) 450+10°C

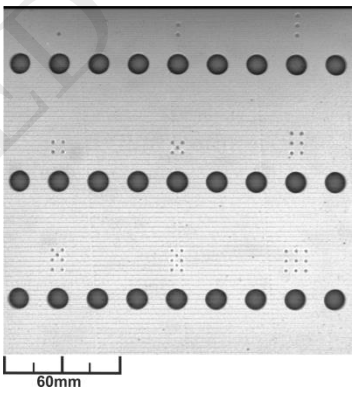


(e) 650+10°C

**Fig. 10** 8-bit, 1800 $pixel$ × 1800 $pixel$ ($row$ × $column$) digital electronic images (processed) covering an imaging area of $180mm$ × $180mm$ ($W \times D$) in the EBM machine processing area, generated at various temperatures, with chamber light off

*3.5 Local Image Quality Comparison between Optical and Electronic Images*

This section presents a qualitative comparison on local image quality between an EBM machine optical image and a prototype electronic image. Only a local feature, i.e. the image contrast between the target plate surface and drilled pockets, is examined. The purpose of this comparison is neither to present any statistically significant observations nor advocate the supremacy of electronic images over thermal/optical images on a quantitative basis. This comparison only aims to give an overview on local image quality between the two types of images.

A typical optical image and electronic image captured and generated at 650+10°C are presented as Figs. 11(a) and (c). These two images are annotated with a red line along their bottom rows crossing the drilled pockets. Figs. 11(b) and (d) are the pixel value profiles along their red lines.

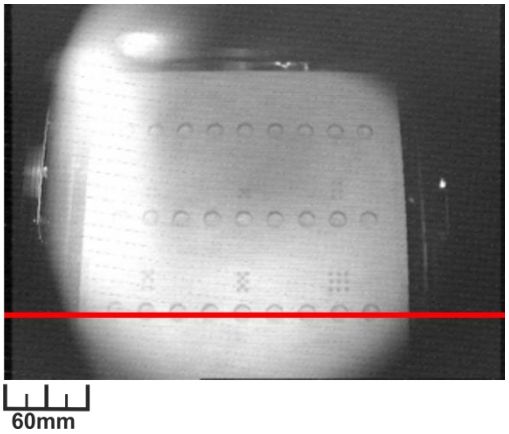


(a) Optical image

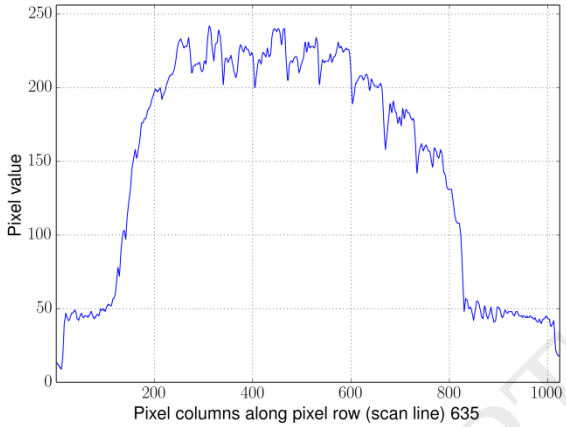


(b) Pixel values along the red line (optical)

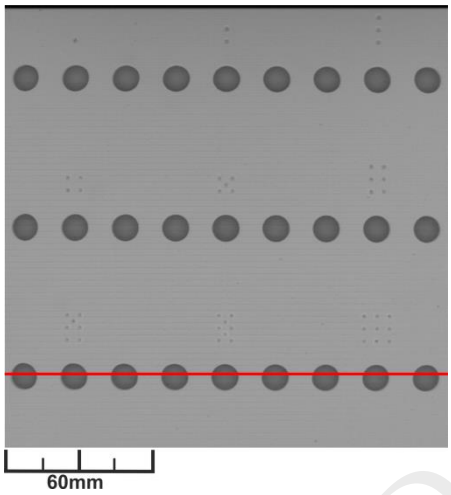


(c) Electronic image (raw)

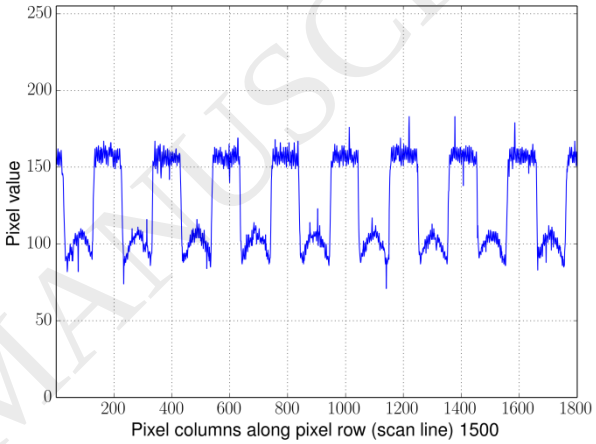


(d) Pixel values along the red line (electronic)

**Fig. 11** Optical and electronic images taken at 650+10°C, with light on

*3.6 Global Image Quality Measure Q Evaluation on Electronic Images*

The influence of temperature on electronic image was investigated, and quantitative analysis on the global quality of electronic images generated at various elevated temperatures was carried out. Reiter et al [36] describe an image quality measure Q in their studies on histogram-based images, as defined by Eq. 7 and Fig. 12.

$$Q = \frac{|\mu_2 - \mu_1|}{\sqrt{\sigma_1^2 + \sigma_2^2}} \tag{7}$$

Where

Q is the image quality measure, $\mu_i$ is the within-class mean, $i = 1, 2$, the pixel value class present, and $\sigma_i$ is the within-class standard deviation, $i = 1, 2$, the pixel value class present

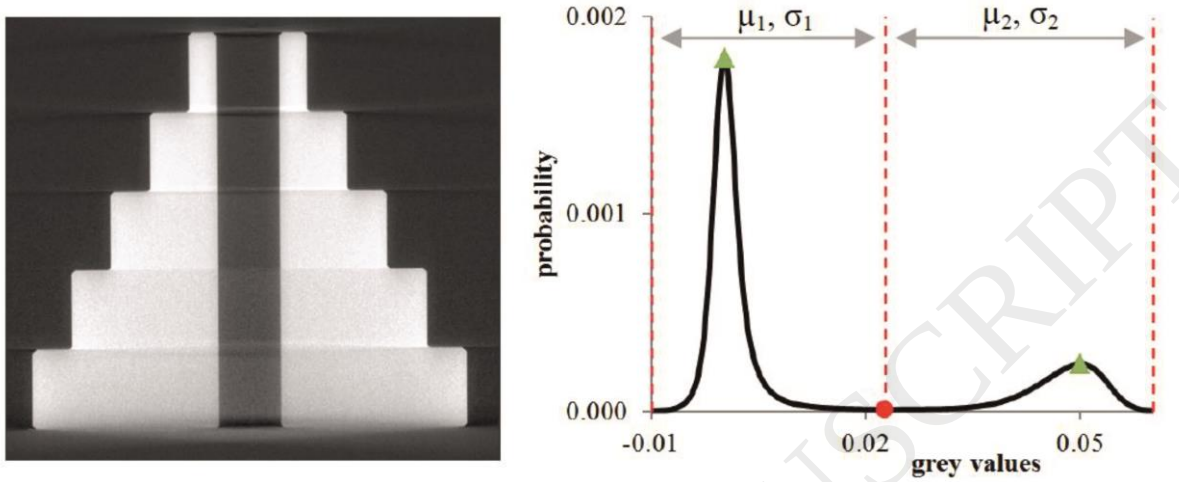


**Fig. 12** A demonstration image and its bimodal histogram showing the definitions of threshold, within-class mean and within-class standard deviation [36]

This image quality measure Q represents the degree of separation between the two pixel value classes in the histogram of interest. An image of ideal global quality is defined to consist of minimum noise and blur throughout the whole image. The separation of the classes within this histogram are maximised whilst the classes' within-class standard deviations are minimised. As the measure Q takes into account both noise and blur, it gives a global impression of image quality. The greater the Q value, the better the global image quality.

A total of ten sets of histograms were assessed in this Q value evaluation. Five sets were generated from raw electronic images while the other five from processed electronic images. Each set contains five histograms. Table 5 and 6 summarise the formation of the ten histogram sets.

**Table 5** The five raw histogram sets involved in image quality measure Q analysis

| Histogram Set | Number of Histograms in a Set | Representative Figure | Temperature / $°C$ |
|---|---|---|---|
| Raw_30 | 5 | 9(a) | 30+10 |
| Raw_200 | 5 | 9(b) | 200+10 |
| Raw_350 | 5 | 9(c) | 350+10 |
| Raw_450 | 5 | 9(d) | 450+10 |
| Raw_650 | 5 | 9(e) | 650+10 |

**Table 6** The five processed histogram sets involved in image quality measure Q analysis

| Histogram Set | Number of Histograms in a Set | Representative Figure | Temperature / $°C$ |
|---|---|---|---|
| Procssed_30 | 5 | 10(a) | 30+10 |
| Processed_200 | 5 | 10(b) | 200+10 |
| Processed_350 | 5 | 10(c) | 350+10 |
| Processed_450 | 5 | 10(d) | 450+10 |
| Processed_650 | 5 | 10(e) | 650+10 |

Otsu thresholding [37] was applied to the ten histogram sets to estimate their pixel value classification thresholds. Thresholding was then followed by the analysis of global image quality measure Q of the histograms. The optical images obtained from the EBM machine camera were not involved in this image quality analysis. These optical images were poor in quality and thus the comparison between them and the electronic images would not provide useful insights. The quality measure Q is a metric based on image contrast. The electronic

images had their image contrast shown between the target plate and the pockets on the plate, as shown in Figs. 13(a)-(d). On the contrary, despite the best effort to improve the quality of the optical images (irrelevant surrounding area beyond target plate cropped out and keystone distortion corrected), these optical images still suffered from the reflection of the chamber light. This led to the image contrast shown between the light reflection and the target plate, as shown in Figs. 13(e)-(h). As the optical and electronic image sets each had image contrast between different objects / features, the comparison on the global image quality measure Q between them is deemed meaningless.

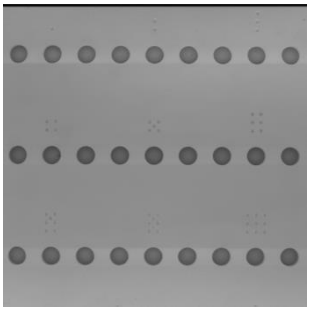

(a) Raw electronic image, 30+10°°C

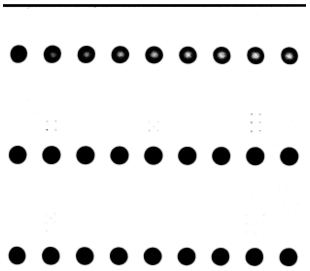

(b) Thresholded electronic image, 30+10°C

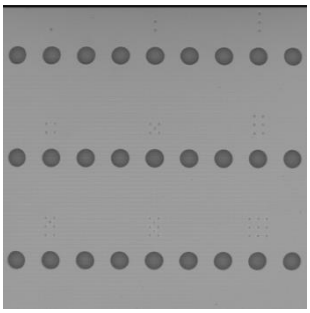

(c) Raw electronic image, 650+10°C

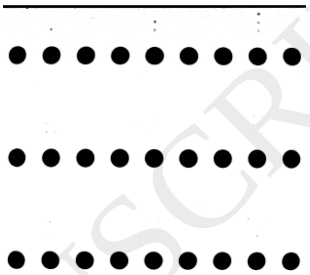

(d) Thresholded electronic image, 650+10°C

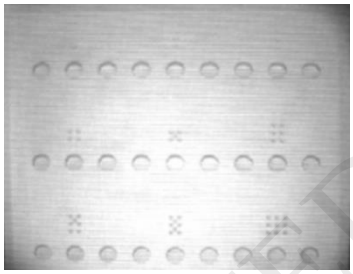

(e) Corrected raw optical image, 30+10°C

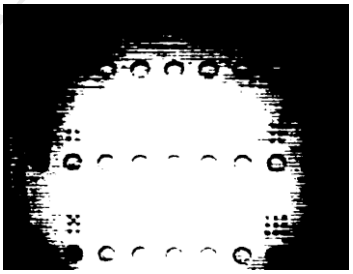

(f) Thresholded optical image, 30+10°C

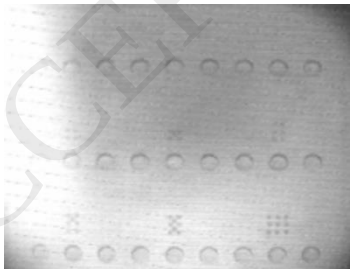

(g) Corrected raw optical image, 650+10°C

(h) Thresholded optical image, 650+10°C

**Fig. 13** Typical optical and electronic images and their thresholded images

Results of the Q values are summarised in Table 7 and 8. The average within-class pixel value means ($\mu_{,avg}$), average within-class standard deviations ($\sigma_{,avg}$), average Q ($Q_{avg}$) values and standard errors are presented. Fig. 14 is a visual representation of results in Table 7 and 8. Although the standard errors are plotted as error bars on Fig. 14, due to their low values, they are not visible. Fig. 14 indicates that the processed electronic images have lower Q values, i.e. poorer global image quality, when compared to that of raw images. From a qualitative perspective, a slight increase in Q values can be observed in both raw and processed images, with increasing imaging temperature.

**Table 7** Global image quality measure Q analyses. Data rounded to 3 s.f.

| Histogram Set | $\mu_{1,avg}$ | $\mu_{2,avg}$ | $\sigma_{1,avg}$ | $\sigma_{2,avg}$ | $Q_{avg}$ | Standard Error |
|---|---|---|---|---|---|---|
| Raw_30 | 86.8 | 146 | 26.5 | 8.07 | 2.12 | 0.0193 |
| Raw_200 | 84.3 | 142 | 24.5 | 6.02 | 2.30 | 0.00355 |
| Raw_350 | 87.1 | 147 | 24.5 | 6.75 | 2.36 | 0.00200 |
| Raw_450 | 86.2 | 148 | 23.9 | 7.34 | 2.46 | 0.00223 |
| Raw_650 | 87.6 | 3.03 | 24.3 | 7.71 | 2.52 | 0.01334 |

**Table 8** Global image quality measure Q analyses. Data rounded to 3 s.f.

| Histogram Set | $\mu_{1,avg}$ | $\mu_{2,avg}$ | $\sigma_{1,avg}$ | $\sigma_{2,avg}$ | $Q_{avg}$ | Standard Error |
|---|---|---|---|---|---|---|
| Processed_30 | 112 | 198 | 34.7 | 27.3 | 1.95 | 0.0187 |
| Processed_200 | 110 | 194 | 38.3 | 27.5 | 1.77 | 0.00322 |
| Processed_350 | 108 | 199 | 39.1 | 26.2 | 1.94 | 0.0102 |
| Processed_450 | 95.0 | 200 | 39.6 | 27.2 | 2.19 | 0.00957 |
| Processed_650 | 95.6 | 204 | 39.9 | 26.5 | 2.25 | 0.00652 |

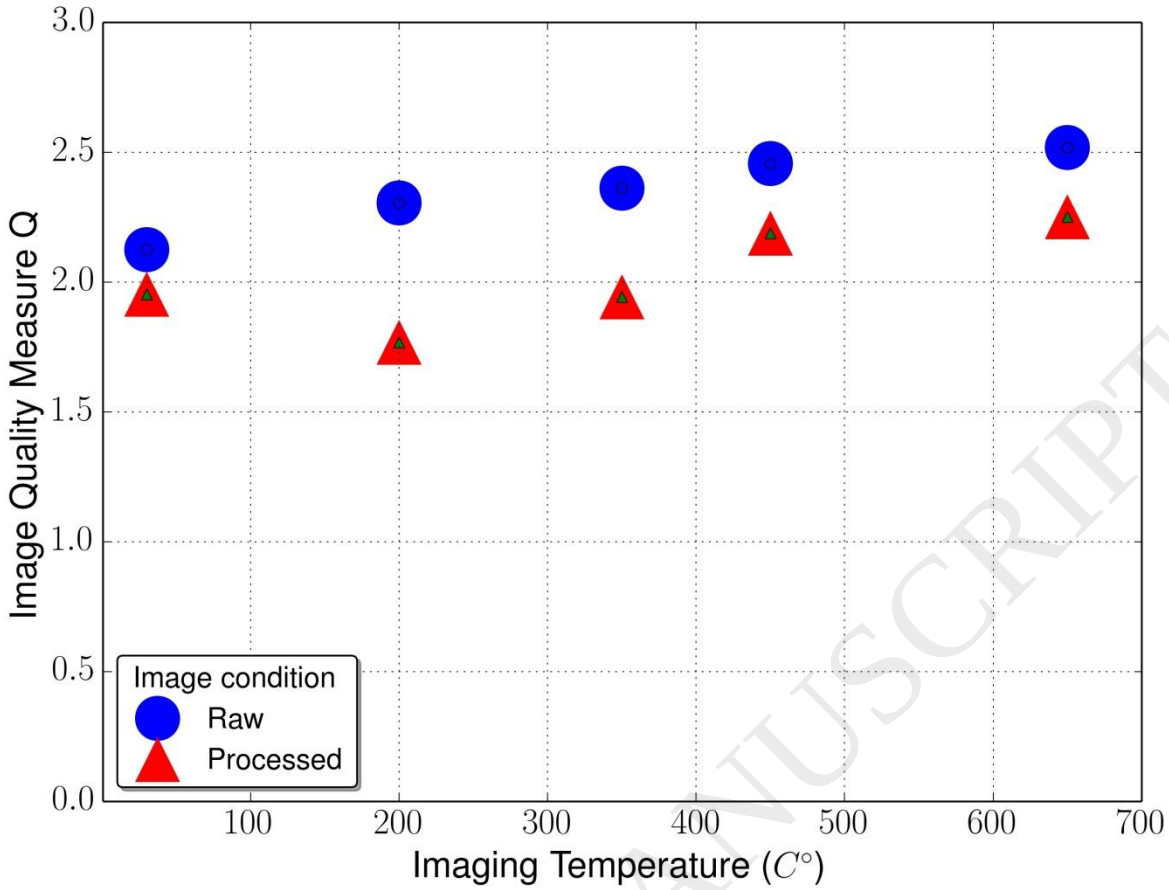


**Fig. 14** A Global image quality measure Q of raw and processed electronic images generated at various elevated temperatures

## 4. Discussion

*4.1 Digital Image Generation at Elevated Temperatures*

Fig. 7 shows the target plate temperature profile measured. Cooling (indicated by negative gradients) is observed from Fig. 7 when electronic imaging is carried out. Moreover, the cooling rate increases (greater gradient, steeper slope) as the target temperature increases. Firstly, this suggests that the target plate struggles to maintain a constant temperature during the experiment. The EBM machine has a controlled vacuum system in which helium gas is admitted into the machine to maintain the $10^{-3}mbar$ operational chamber pressure as described in Table 4. It is thought that during controlled heating of the target plate, heat was lost to the machine chamber and the machine surrounding via convection and conduction. According to Newton's law of cooling (Eq. 8 [38]), the heat transfer rate $\dot{Q}_{conv}$ increases

with an increasing temperature difference. As the target plate becomes hotter, the temperature difference between itself and the machine chamber and surrounding environment increases, thus leading to a greater $\dot{Q}_{conv}$. As the amount of activity carried out during each imaging trial (as described in Section 2.3) is the same, it is expected that the time involved in imaging will be similar. With similar imaging time and an increasing $\dot{Q}_{conv}$ at higher temperature, the temperature drops are expected to be greater at higher temperatures. The profile of the target plate depicted in Fig. 7 has been explained.

$$\dot{Q}_{conv} = hA(T_s - T_f) \tag{8}$$

Where

$\dot{Q}_{conv}$ is the heat transfer rate by convection, h is the convection heat transfer coefficient

A is the surface area involved in heat transfer, and Ti is the temperature of s = surface and f = bulk fluid, $i = s, f$

*4.2 Electronic Images from the Prototype*

Figs. 9(a)-(e) and Figs. 10(a)-(e) are the typical raw and processed electronic images generated at various elevated temperatures. A black line is present at the top of all raw and processed images. Delays in the delivery of electron beam current from the EBM machine electron gun is thought to be the root cause, as mentioned in literature [22].

Figs. 10(a) and (b) show a darker middle area when compared to the rest of the image areas. This observation suggests a difference in surface texture between the middle and the rest of the target plate. It is thought that the texture variation comes from the manual bead blasting described in Section 2.2. Bead blasting was focused on the middle of the target plate, in order to smooth out the horizontal markings left behind from the developmental trials prior to the imaging experiment. Figs. 10(c)-(e) do not contain any dark areas in the middle of the plate. In Fig. 7, the target plate temperature profile shows that the plate goes through multiple heating sequences for 0.6+0.1, 0.9+0.1 and 1.3+0.1 hours before reaching temperature of 350+10°C, 450+10°C and 650+10°C, when Figs. 10(c)-(e) were generated. It is thought that the controlled heating via electron beam scanning modified the target plate surface texture throughout the experiment, smoothing out the variation in surface texture. This argument is supported by the fact that horizontal markings across the target plate become more and more

visible from Figs. 10(a)-(e), as the imaging temperature increases. As a result, the surface texture variation due to bead blasting at the start of the experiment is no longer present, by the time that images shown in Figs. 10(c)-(e) were generated.

*4.3 Comparison between Optical Images and Electronic Images*

Figs. 8(a)-(d) are EBM machine computer screenshots of optical images taken by the machine camera at 30+10°C (Figs. 8(a) and (b)) and 650+10°C (Figs. 8(c) and (d)). The bright spots in Figs. 8 (a) and (c) are thought to be attributed to incandescence of the electron gun cathode. The EBM machine has a thermionic electron gun [39], and when the tungsten cathode is heated, it emits blackbody radiation according to Planck's law [40]. The bright spot in Fig. 8(c) is less visible as the target plate is brighter when compared to that in Fig. 8(a). This occurs when the target plate is at 650+10°C, and glows as predicted by Planck's law. When the machine chamber light was turned on, the image contrast due to incandescence was less obvious, as demonstrated by Figs. 8(b) and (d). The effect of cathode incandescence is thought to be a potential issue with thermal / optical imaging systems. These systems rely on the correct operation of the machine chamber light. If the chamber light malfunctions, the quality of the images captured during in-process data collection is compromised.

Figs. 9(a)-(e) show typical raw digital electron images generated at a range of temperatures, with the chamber light switched off. These images demonstrate that cathode incandescence does not influence the electronic image quality. This occurs because the energy of the electron cathode blackbody radiation is caused by photons, the electron sensor in the prototype only registers electrons impinging onto its sensing surface. This blackbody radiation is invisible to the electronic imaging system.

In comparison with optical images of Figs. 8(a)-(d), the image FOV of the digital electronic images of Figs. 9(a)-(e) only consist of a user-defined 180 mm ×180 mm (W×D) Regions of Interest (ROI), without including any other monitoring-irrelevant regions beyond the machine processing area. Thus, all image pixels are carrying useful information for monitoring.

When compared with the optical image of Fig. 11(a), the electronic image of Fig. 11(c) reveals more topographical details of the target plate. Fig. 11(c) shows the drilled pockets with greater clarity when compared to Fig. 11(a). From a qualitative perspective, this

observation is supported by Fig. 11(d), the contrast in pixel value is better-defined when compared to that in Fig. 11(b).

*4.4 Global Image Quality Measure Q of Electronic Images at Elevated Temperatures*

A total of ten sets of histograms (five images per set) were assessed in the Q value evaluation. Fig. 14, in which standard errors are plotted as error bars, shows that the standard errors of all images involved are insignificant as the error bars are not visible. This indicates that for each image set, the five electronic images generated at each elevated temperature are similar in quality.

Fig. 14 demonstrates that the Q values of raw images are greater than that of the processed images. This indicates that global image quality of the raw images is higher. As discussed in Section 3.3, processed images are generated by applying noise removal and contrast enhancement to the raw images. The contrast enhancement amplifies the local pixel intensity variations in the raw images. Although the enhancement leads to greater difference between the two within-class means ($\mu_1$ and $\mu_2$), the sum of the within-class standard deviations ($\sigma_1$ and $\sigma_2$) are even greater. Thus, the resultant Q value drops after image processing is carried out (refer to Eq. 7).

Still referring to Fig.14, a gradual increase in Q value with higher imaging temperature can be observed for both raw and processed images, indicating that the global image quality increases with higher temperature. This phenomenon is thought to be mainly due to the undesired surface texture variation across the target plate at the start of the experiment. As referenced in Section 2.2 and 4.2, the electron beam scanning motion during controlled heating is believed to have modified the target plate surface texture. As the experiment proceeds, more electron beam scanning is carried out, bringing up the target plate temperature, and the initial target plate surface texture variation becomes smoother. Consequently, with higher imaging temperature, the global image quality improves.

In this study, contrary to the observations made by Nakamura et al [31] and Gregori et al [32], no observable reduction in electronic image SNR (Q value as indicator) was recorded at elevated temperatures. Nakamura et al and Gregori et al conducted their high temperature imaging studies with a JEOL JSM-845 Scanning Electron Microscope (SEM) and a JEOL JSM 6400 SEM respectively. The typical chamber pressure of these SEMs is at $1x10^{-5}$mbar [41]. The Arcam EBM A1 machine typical chamber pressure is at $2x10^{-3}$mbar due to the

presence of helium gas. It is thought that, in this study, the helium gas suppressed the movements of any undesired thermionic electrons emitted from the imaging target. Similar to the situation in environmental/ variable pressure SEM, it is expected that the helium gas molecules in the Arcam EBM machine got ionised by the primary electron beam and the feedback electrons emitted from the imaging target. It is postulated that these positively charged ions absorbed and neutralised [42] the negatively charged, low energy thermionic electrons and prevented them from reaching the electron sensor. In addition, whilst Nakamura et al [31] used a primary electron beam current of 1nA for imaging, the primary electron beam current used in this study was 1mA, which is 1,000,000 times greater. It is thought that the ratio of useful feedback electron signal for imaging to the thermionic electron noise in this study was much greater than that in the study carried out by Nakamura et al. As a result, the electronic image SNR was not affected by temperature in this study.

## 5. Conclusions

Electron signal amplifier modification, controlled heating software development and experimental setup for carrying out electronic imaging trials at elevated temperatures have been presented. Optical (Arcam A1 EBM machine chamber camera) and electronic images (self-developed prototype) were captured and generated at temperatures covering a range of $30°C$ to $650°C$. When compared with optical images, electronic images show that they have better-defined image FOV, and are not affected by cathode incandescence. Global image quality measure Q analysis was carried out on both raw and processed electronic images to evaluate the influence of temperature on image quality. Electronic images generated in the experiment have low standard error, showing that their image quality is consistent. Moreover, electronic images generated at higher temperatures have greater Q value, i.e. better global image quality. This difference is mainly attributed to the undesired surface texture variation of the imaging target due to electron beam heating. At the start of the experiment, the imaging target contained an undesirable, inhomogeneous surface texture. Scanning of the electron beam during heating is thought to have homogenised the surface texture, thus leading to higher Q values of images. It has been demonstrated that, for temperature in the range from 30°C to 650°C, the influence of temperature on electronic image quality is minimal. It is envisaged that the prototype under test has significant potential to contribute to in-process EBM monitoring in many manufacturing sectors, including the aerospace and medical device industries.

There will, however, be challenges ahead in order to realise the prototype potential. Future studies will focus on these issues which include: (1) carrying out electronic imaging on multi-layer for the whole additive manufacturing process, (2) further develop the current electronic imaging system prototype to meet industrial standards. For instance, National Instruments data logger should be considered to speed up the data logging rate to 3.24MHz (26Mbps) to bring down the current image frame time from 27s to 1s, in order to minimise the extra EBM layer time incurred due to imaging, and (3) resolving potential sensor issues due to metallisation generated from vaporisation of metal powder during the EBM process. No metallisation was observed visually in this study as no powder was deposited onto the processing area and no components were manufactured in the experiments. Nevertheless, during a real EBM build, metallic vapour is expected to deposit onto the signal capturing surfaces of the electron sensor. Gaps might form between the metallisation thin film and the sensor surface, and might lead to an increase in the local electrical resistance, which in turn, might induce undesired and observable feedback electron signal variation, leading to undesired local image contrast.

## Acknowledgements

*The Author(s) declare(s) that there is no conflict of interest. This research received no specific grant from any funding agency in the public, commercial, or not-for-profit sectors. The EBAM machine was purchased, in part from a grant received for the EPSRC Centre for Innovative Manufacturing in Additive Manufacturing.*

## References

1. I. Gibson, D.W. Rosen, B Stucker (2010) Additive Manufacturing Technologies. Springer, New York, pp. 126-128

2. X Gong, T Anderson, K Chou (2014) Review on Powder-Based Electron Beam Additive Manufacturing Technology. Manufacturing Review 1 2. DOI: 10.1051/mfreview/2014001

3. O.L.A Harrysson, O. Cansizoglu, D.J. Marcellin-Little, D.R Cormier, H.A West (2008) Direct Metal Fabrication of Titanium Implants with Tailored Materials and Mechanical Properties using Electron Beam Melting Technology, Materials Science and Engineering: C, Volume 28, Issue 3, 2008, Pages 366-373, ISSN 0928-4931, http://dx.doi.org/10.1016/j.msec.2007.04.022.

4. G. Baudana, S. Biamino, D. Ugues, M. Lombardi, P. Fino, M. Pavese, C. Badini, (2016) Titanium Aluminides for Aerospace and Automotive Applications Processed by Electron Beam Melting: Contribution of Politecnico di Torino, Metal Powder Report, Volume 71, Issue 3, 2016, Pages 193-199, ISSN 0026-0657, http://dx.doi.org/10.1016/j.mprp.2016.02.058.

5. J.P. Jarow, J.H. Baxley (2015) Medical devices: US Medical Device Regulation, Urologic Oncology: Seminars and Original Investigations, Volume 33, Issue 3, March 2015, Pages 128-132, ISSN 1078-1439, https://doi.org/10.1016/j.urolonc.2014.10.004.

6. L. Portolés, O. Jordá , L. Jordá, A. Uriondo, M. Esperon-Miguez, S. Perinpanayagam (2016) A qualification Procedure to Manufacture and Repair Aerospace Parts with Electron Beam Melting, Journal of Manufacturing Systems, Volume 41, 2016, Pages 65-75, ISSN 0278-6125, http://dx.doi.org/10.1016/j.jmsy.2016.07.002.

7. M. Mani, B. Lane, A. Donmez, S. Feng, S. Moylan, R. Fesperman (2015) NISTIR 8036. Measurement Science Needs for Real-time Control of Additive Manufacturing Powder Bed Fusion Processes. http://dx.doi.org/10.6028/NIST.IR.8036

8. J. Raplee, A. Plotkowski, M.M. Kirka, R. Dinwiddie, A. Okello, R.R. Dehoff, S.S Babu (2017) Thermographic Microstructure Monitoring in Electron Beam Additive Manufacutirng, Scientific Reports 7, Article Number: 43554. doi:10.1038/srep43554

9. P.M. Cordero, J. Mireles, S. Ridwan, R.B. Wicker (2017) Evaluation of Monitoring Methods for Electron Beam Melting Powder Bed Fusion Additive Manufacutirng Technology, Progress in Additive Manufacturing, June 2017, Volume 2, Issue 1-2, pp 1-10, https://doi.org/10.1007/s40964-016-0015-6

10. E. Rodriguez, F. Medina, D. Espalin, C. Terrazas, D. Muse, C. Henry, E. MacDonald, R. Wicker (2012) Integration of a Thermal Imaging Feedback Control System in Electron Beam Melting, Proceedings from the Solid Freeform Fabrication Symposium, pp 945–961

11. J.N. Zalameda, E.R. Burke, R.A. Hafley, K.M.B. Taminger, C.S. Domack, A. Brewer, R.E. Martin (2013) Thermal Imaging for Assessment of Electron-Beam Freeform Fabrication Additive Manufacturing Deposits, Proceeding of SPIE, Volume 8705, Thermosense: Thermal Infrared Applications XXXV, 87050M (2013), doi: 10.1117/12.2018233

12. S. Price, J. Lydon, K. Cooper, K Chao (2013) Experimental Temperature Analysis of Powder-Based Electron Beam Additive Manufacturing, Proceedings from the Solid Freeform Fabrication Symposium, pp. 162-173

13. S. Price, K. Cooper, K. Chou (2012) Evaluations of Temperature Measurmnets by Near-Infrared Thermography in Powder-Based Electron-Beam Additive Manufacturing, Proceedings from the Solid Freeform Fabrication Symposium, pp. 761-773

14. T. Scharowsky, A. Bauereiß, R.F. Singer, C. Körner (2012) Observation and Numerical Simulation of Melt Pool Dynamic and Beam Powder Interaction During Selective Electron Beam Melting, Proceedings from the Solid Freeform Fabrication Symposium, Austin, pp 815–820

15. S. Ridwan, J. Mireles, S.M. Gayton, D. Espalin, R.B. Wicker (2014) Automatic Layerwise Acquisition of Thermal And Geometric Data of The Electron Beam Melting Process Using Infrared Thermography, Proceedings from the Solid Freeform Fabrication Symposium, pp 343–352

16. J. Mireles, S. Ridwan, P.A. Motron, A. Hinojos, R.B. Wicker (2015) Analysis and Correction of Defects Within Parts Fabricated Using Powder Bed Fusion Technology. Surface Topography: Metrology and Properties, Volume 3, Number 3. doi:10.1088/2051-672X/3/3/034002

17. R.B. Dinwiddie, R.R. Dehoff, P.D. Lloyd, L.E. Lowe, J.U.B Ulrich (2013) Thermographic In-Situ Process Monitoring of the Electron-Beam Melting Technology Used in Additive Manufacturing, Proceeding of SPIE, Thermosense: Thermal Infrared Applications XXXV, 87050K; doi:10.1117/12.2018412

18. J. Schwerdtfeger, R.F. Singer, C. Körner (2012) In situ flaw detection by IR-imaging during electron beam melting, Rapid Prototyping Journal, Vol. 18 Issue: 4, pp.259-263, https://doi.org/10.1108/13552541211231572

19. J. Mireles, C. Terrazas, S.M. Gaytan, D.A. Roberson, R.B. Wicker (2015) Closed-Loop Automatic Feedback Control in Electron Beam Melting, Int J Adv Manuf Technol. 78: 1193. doi:10.1007/s00170-014-6708-4

20. J. Mireles, C. Terrazas, F. Medina, R. Wicker (2013) Automatic Feedback Control in Electron Beam Melting Using Infrared Thermography. Proceedings from the Solid Freeform Fabrication Symposium, Austin, pp 708–717

21. H. Wong, D. Neary, E. Jones, P. Fox, C. Sutcliffe (2018) Pilot capability evaluation of a feedback electronic imaging system prototype for in-process monitoring in electron beam additive manufacturing, Springer International Journal of Advanced Maufacturing Technology, in-press, DOI: 10.1007/s00170-018-2702-6

22. H. Wong, D. Neary, S. Shahzad, E. Jones, P. Fox, C. Sutcliffe (2018) Pilot Investigation of Feedback Electronic Image Generation in Electron Beam Melting and its Potential for In-Process Monitoring, Elsevier Journal of Materials Processing Technology, in-press, DOI: 10.1016/j.jmatprotec.2018.10.016

23. A. Dinh (2005) Noise and Noise Reduction Techniques, EE 323.3 Electronic Instrumentation teaching materials, College of Engineering, University of Saskatchewan, Canada

24. B. Dutta, F.H. Froes (2017) The Additive Manufacturing (AM) of titanium alloys, Metal Powder Report, Volume 72, Issue 2, pp. 96-106, ISSN 0026-0657, https://doi.org/10.1016/j.mprp.2016.12.062

25. M.J. Donachie (1988) Titanium; A Technical Guide. ASM International, pp. 31

26. A. Kirchner,B. Klöden, L. Luft, T. Weißgärber, B. Kieback (2014) Process Window for Electron Beam Melting of Ti-6Al-4V, Proceeding of EuroPM 2014 – AM Technologies

27. H. Bruining (1954) Physics and Applications of Secondary Electron Emission. London Pergamon Press Ltd, pp. 88

28. L. Reimer (1998) Scanning Electron Microscopy: Physics of Image Formation and Microanalysis, Springer, pp. 4 – 5

29. Arcam A1 EBM Machine Specification, Arcam AB

30. J.I. Goldstein, D.E. Newbury, J.R. Michael, N.W.M. Ritchie, J.H.J Scott, D.C. Joy (2018) Scanning Electron Microscopy and X-Ray Microanalysis (Forth Edition). Springer, pp. 30

31. M. Nakamura, T. Isshiki, M. Tamai and K. Nishio (2002) Development of a New Heating Stage Equipped Thermal Electron Filter for Scanning Electron Microscopy, Proc. 15th International Congress on Electron Microscopy, Durban, South Africa

32. G. Gregori, H.J Kleebe, F. Siegelin, G. Ziegler (2002) In Situ SEM Imaging at Temperatures as High as 1450°C, Journal of Electron Microscopy, Vol. 51 No.6: 347-352

33. H.B Michaelson (1950) Work Functions of the Elements, Journal of Applied Physics 21, 536; https://doi.org/10.1063/1.1699702

34. Lecture 2: Electrical Resistivity of Materials, Teaching Materials, Al-Mustansiriya University (https://uomustansiriyah.edu.iq/media/lectures/5/5_2016_05_01!04_07_34_PM.pdf)

35. R.C. Gonzalez, R.E. Woods (2008) Digital Image Processing, Pearson Eductaion, Inc., pp. 122-127, 322-327

36. M. Reiter, D. Weiss, D, C. Gusenbauer, M. Erler, C. Kuhn, S. Kasperl, J. Kastner (2014) Evaluation of a Histogram-Based Image Quality Measure for X-ray Computed Tomography, Proceedsing of Conference on Industrial Computed Tomography 2014

37. N. Otsu (1979) A Threshold Selection Method from Gray-Level Histograms, IEEE Transactions on Systems, Man, and Cybernetics, Vol. SMC-9, No.1

38. T.A. Çengel, M.A. Boles (2011) Thermodynamics (Seventh Edition). McGraw Hill, pp. 93

39. B. Wysocki, P. Maj, R. Sitek, J. Buhagiar, K.J. Kurzydłowski, W. Święszkowski (2017) Laser and Electron Beam Additive Manufacturing Methods of Fabricating Titanium Bone Implants. Applied Sciences. 2017; 7(7): 657. https://doi.org/10.3390/app7070657

40. P.K. Jain, L.K. Sharma (1998) The Physics of blackbody radiation: A review, Journal of Applied Science in Southern Africa 4(2):80-101, DOI: 10.4314/jassa.v4i2.16899

41. JEOL. SEM Scanning Electron Microscope A to Z: Basic Knowledge for Using the SEM. Pages: 23-26

42. A. Mohan, N. Khanna, J. Hwu, D.C. Joy (1998) Secondary Electron Imaging in the Variable Pressure Scanning Electron Microscope, Scanning Vol. 20, pp. 436-441